

Internal structure of bilobate comets revealed by erosion from shear deformation

C. Matonti^{1,2*}, N. Attree^{1,3}, O. Groussin¹, L. Jorda¹, S. Viseur², S. Hviid⁴, S. Bouley⁵, D. Nébouy¹, A-T. Auger¹, P. Lamy^{1,6} and, H. Sierks⁷, G. Naletto^{8,9,10}, R. Rodrigo^{11,12}, D. Koschny¹³, B. Davidsson¹⁴, M. A. Barucci¹⁵, J.-L. Bertaux⁶, I. Bertini⁸, D. Bodewits¹⁶, G. Cremonese¹⁷, V. Da Deppo¹⁰, S. Debei¹⁸, M. De Cecco¹⁹, J. Deller⁷, S. Fornasier¹⁵, M. Fulle²⁰, P. J. Gutiérrez²¹, C. Güttler⁷, W.-H. Ip^{22,23}, H. U. Keller^{24,4}, L. M. Lara²¹, F. La Forgia⁸, M. Lazzarin⁸, A. Lucchetti¹⁷, J. J. López-Moreno²¹, F. Marzari⁸, M. Massironi^{25,9}, S. Mottola⁴, N. Oklay⁴, M. Pajola¹⁷, L. Penasa⁹, F. Preusker⁴, H. Rickman^{26,27}, F. Scholten⁴, X. Shi⁷, I. Toth²⁸, C. Tubiana⁷, J.-B. Vincent⁴.

1 : Aix Marseille Univ, CNRS, CNES, LAM, Marseille, France, 2 : Aix-Marseille Université, CEREGE, IRD, CNRS, Ressources, Réservoirs et Hydrosystèmes/Terre et planète, Marseille, France, 3 : Faculty of natural sciences, University of Stirling, Stirling, UK, 4 : Deutsches Zentrum für Luft- und Raumfahrt (DLR), Institut für Planetenforschung, Rutherfordstraße 23, 12489 Berlin, Germany. 5 : GEOPS—Géosciences Paris Sud, Université Paris-Sud, CNRS, Université Paris-Saclay, Rue du Belvédère, Bâtiment 504-509, 91405 Orsay, France. 6 : LATMOS, CNRS/UVSQ/IPSL, 11 Boulevard d'Alembert, 78280 Guyancourt, France., 7: Max Planck Institute for Solar System Research, Justus-von-Liebig-Weg 3, 37077 Göttingen, Germany. 8: University of Padova, Department of Physics and Astronomy “Galileo Galilei”, Via Marzolo 8, 35131 Padova, Italy. 9 : University of Padova, Center of Studies and Activities for Space (CISAS) “G. Colombo”, Via Venezia 15, 35131 Padova, Italy. 10 : CNR-IFN UOS Padova LUXOR, Via Trasea 7, 35131 Padova, Italy. 11 : Centro de Astrobiología, CSIC-INTA, 28850 Torrejón de Ardoz, Madrid, Spain. 12: International Space Science Institute, Hallerstrasse 6, 3012 Bern, Switzerland. 13 : Science Support Office, European Space Research and Technology Centre/ESA, Keplerlaan 1, Postbus 299, 2201AZ Noordwijk ZH, The Netherlands. 14 : Jet Propulsion Laboratory, M/S 183-401, 4800 Oak Grove Drive, Pasadena, CA 91109, USA. 15 : LESIA, Observatoire de Paris, Université PSL, CNRS, Univ. Paris Diderot, Sorbonne Paris Cité, Sorbonne Université, 5 Place J. Janssen, 92195 Meudon Principal Cedex, France. 16 : Physics Department, Auburn University, Auburn AL 36849, USA. 17 : INAF, Astronomical Observatory of Padova, Vicolo dell'Osservatorio 5, 35122 Padova, Italy. 18 : University of Padova, Department of Industrial Engineering, Via Venezia 1, 35131 Padova, Italy. 19: University of Trento, Faculty of Engineering, Via Mesiano 77, 38121 Trento, Italy. 20 : INAF Astronomical Observatory of Trieste, Via Tiepolo 11, 34143 Trieste, Italy. 21 : Instituto de Astrofísica de Andalucía (CSIC), c/ Glorieta de la Astronomía s/n, 18008 Granada, Spain. 22 : Graduate Institute of Astronomy, National Central University, 300 Chung-Da Rd, Chung-Li 32054,

Taiwan. 23 : Space Science Institute, Macau University of Science and Technology, Avenida Wai Long, Taipa, Macau. 24 : Institut für Geophysik und extraterrestrische Physik, Technische Universität Braunschweig, Mendelssohnstr. 3, 38106 Braunschweig, Germany. 25 : University of Padova, Department of Geosciences, Via G. Gradenigo 6, 35131 Padova, Italy. 26: Department of Physics and Astronomy, Uppsala University, Box 516, 75120 Uppsala, Sweden. 27 : PAS Space Research Center, Bartycza 18A, 00716 Warszawa, Poland. 28 : Konkoly Observatory, PO Box 67, 1525 Budapest, Hungary.

Comets are icy bodies, eroding with time by losing gas and dust. While nucleus erosion by ice-sublimation has been long-known, shaping processes are still a debated question, where the importance of geological processes and structures remains mainly unknown. Here we reveal, with the example of 67P, the existence of significant mechanically-driven erosion on bilobate comets. It originates from a shear deformation process in the neck, possibly active over Gyr's, and mostly independent from the Sun distance. We report on how shear fracture and fault networks, characterized here for the first time, contributed to the nucleus mechanical erosion and how they explain 67P's strongly marked neck trough. Our 3D analysis proves that the nucleus interior is structured by decameter-to-hectometer shear-fracture networks, propagating ≥ 500 m below the surface, in a mechanically homogeneous material. This erosion process, guided by fractures, is generic and could apply to other bilobate comets, due to their peculiar geometry. It is a dominant process to shape the surface and structure the interior of bilobate comets, possibly even during their residence-time in the outer solar system, where water ice sublimation is negligible.

Following classical dynamical scenarios¹, comets were formed during the early stages of the solar system, and have been since stored far from the Sun in a very cold environment, either in the Kuiper belt or the Oort cloud. They hold clues to constrain the formation and evolution of the solar system, including insights into prebiotic molecular chemistry. Comet 67P/Churyumov-Gerasimenko (hereafter 67P), studied here, is a Jupiter family comet that originates from the Kuiper Belt.

During its two years orbiting comet 67P, Rosetta's cameras have acquired thousands of images revealing its bilobate nature². Bilobate comets can be formed by, either the low-velocity (meters per second) accretion of two primordial objects^{3,4}, or the re-aggregation of material after a later nucleus rotational breakup⁵ or even catastrophic collision^{6,7} that can happen multiple times. Such a configuration seems to be common for comets, since four of the seven spatially resolved nuclei are bilobate. Understanding erosion processes on cometary nuclei and how these processes modify their global shape is key to constrain their internal structure and evolution.

OSIRIS-NAC⁸ image resolution (down to <20cm/px) allowed for detailed geological interpretations and in particular led to the observation of pervasive arrays of lineaments existing at all scales (from centimeters-to-hectometers), some of which have been interpreted as layers^{2,3} and others as fractures^{9,10,11}. While the meter-scale polygonal fractures originate from thermal stress^{11,12}, a significant population of tens-to-hundreds of metres-scale fractures still remains from unknown origin. Lineaments are mainly observed in the Southern Hemisphere (SH), which exhibits less-to-no dust deposits compared to the Northern Hemisphere (NH)¹³, and therefore more continuous outcrops of brittle material, prone to fracturing (Fig. 1a).

Hectometre to kilometre fracture networks near the neck

In the SH neck and neck-border regions (Fig. 1a and Supplementary Figs. 1 & 3-5) we observed 2 types of tens-to-hundreds of meter long lineaments. Type-1 lineaments (green in Figure 1.) are continuous and parallel to each-other (green arrow in Fig.1c; Fig.1d, and Supplementary Fig. 5). These lineaments follow the topography contour lines and are therefore sub-parallel to the surface (Supplementary information 2.1 and Supplementary Fig. 5 and 7c-d), which agrees well with their previous interpretation and modelling as possible layers^{3,14}.

Type-2 lineaments (red in Fig. 1) are composed of two sets, each with a preferential direction. They show the following attributes: (i) high interconnectivity and bent extremities (Figs. 1b2, 1d2); (ii) discontinuous and curvilinear; (iii) crosscut, hence postdate, type-1 lineaments (Fig. 1d1-1d2). Type-2 lineaments straightly cut across contour lines and are consequently sub-vertical to the surface (Fig 1b-c, Supplementary Figs. 3-4 and 7 and Supplementary information 1.1; 2.1 and 2.2). From these characteristics, and following the geological principles of initial horizontality¹⁵ and cross-cutting relationship¹⁶, type-2 lineaments cannot be primordial features such as layers, but are structural discontinuities, i.e. fractures or faults.

Evidence for shear deformation

In addition to the above basic attributes defining fractures, type-2 lineaments show strong evidences for shearing. Fracture terminations such as branching structures or imbricated-fans observed in the Geb and Atum regions (Fig. 1, Supplementary Figs. 3-4) are typical of fractures or faults developed in a shear context¹⁷ (Figs 1b3,1d3). In the Wosret and Anhur regions at the neck's border, anastomosing fracture pattern with numerous interconnections (Fig.1b-d and Supplementary Fig. 5), along with bends of one fracture extremity toward another, indicate mechanical interaction and also suggest a shear context^{18,19,20} (Supplementary Fig. 3b, Fig. 1b3-

d3). In Sobek and Neith, in the neck's central regions, we observe highly fractured sheared block structures²¹, alternating with unstructured areas composed of meter-scale (possibly less) blocks (Fig. 1c, 1e1-3, Supplementary information 2.3). Possible meter-scale offsets of previously formed lineaments (fractures or layers) in the Geb region clearly point to fault-like planes existing on 67P (Supplementary Fig. 3c and Supplementary information 1).

The evolution of these fracture and fault structures towards the neck's centre, from branching and anastomosing networks in the neck border, to sheared blocks and crushed-chaotic zones in the neck centre (Figs 1c,1e and Supplementary Fig. 6a, Supplementary information 2.3), suggests an increasing deformation gradient. This observation is fully consistent with classical fault/sheared-zone models on Earth, where maximum strain is located at its centre²² (Supplementary Fig. 6b).

If the shearing process is a valid interpretation, fractures patterns should follow geologically significant geometry. To further assess this geometry and reinforce the evidence for shearing, we performed a quantitative analysis of lengths and directions of 2879 fractures. The fracture lengths vary from 0.5 to 450 m. The fracture cumulative length distribution follows a power law between 30 and 250 m, with a power index of -2.3 (Fig. 2a). Such a distribution is typical of fractures and faults on Earth²³, and this index is moreover mainly characteristic of fractures formed and/or reactivated in shear²⁴. The 326 longest fractures (>100 m, Fig. 2c) are all strictly orientated within 35° of the neck midplane direction²⁵ (see methods) and form characteristic diamond-shaped patterns visible in both hemispheres (Supplementary Figs. 7c-d, 8c and 9) following two preferential directions separated by 30-40° (Fig. 2c-d). Such a pattern matches strikingly well with the occurrence of a Riedel-shear deformation structure between the lobes^{26,27,28} that can exist at all scales (Supplementary Figs 8a,8d, and Supplementary information 2.4). The measured 30-40° angle between Riedel-shear fractures should correspond to the internal friction angle of the

material (Supplementary Fig. 8a), which fully agrees with values estimated for 67P using surface morphologies and modeling^{5,29,30}.

Interestingly, the length distribution of the smallest (<30 m) fractures doesn't follow a power law, as well as the polygonal meter-scale fractures (Fig. 2b), and shows a large scattering in directions, of almost 180° (Fig. 2d), which both support a different origin for them³¹, likely thermal fracturing instead of “tectonic-like” shearing.

Finally, a stress model of 67P³² has been developed (see methods), which indicates that the maximum differential stress, of up-to 450 Pa, occurs in the neck regions (Supplementary Fig. 10a). This value exceeds the estimated bulk nucleus (tensile or shear) strength of typically 1-100 Pa^{33,34}, thus allowing fracturing. Shear stress is also maximum near the Neck centre (>100 Pa, Supplementary Fig. 10b) and in the neck's perpendicular direction, which is compatible with the location and directions of the observed shear-deformations. Such a stress is caused by torque at the neck boundary, due to the fact that the neck, plus head-lobe, are cantilevered over 67P's centre of gravity and falling onto it with a twisting motion.

To summarise, all the above observations and models cannot be explained by thermal processes and demonstrate the occurrence of a global shear deformation happening all around the neck, which is mostly independent of solar insulation and has been active far from the sun, possibly over Gyr's⁴, since 67P became bilobate.

Constraining the nucleus internal structure

The global shear stress not only implies surface deformation, but also a strain in the whole nucleus interior. In order to assess this hypothesis, we studied fractures along the vertical direction, relative to the local gravity vector (i.e. along their height instead of their strike), hence probing the nucleus internal structure.

Fractures observed vertically on cliffs in the NH equatorial region (thereafter Bakhu, Supplementary Figs. 7a-b and 9b and Supplementary information 2.4 & 3) show maximum heights of 120-190 m. Considering a maximum length of 450 m, this gives fracture Length/Height ratios around 2.36-3.75 (Fig. 3) typical for fractures and faults on Earth, especially non-layer-restricted ones ($1.8 < L/H < 3.8$ ³⁵).

Fractures on the neck borders (Wosret and Anhur) and neck deepest point (Sobek) exhibit similar patterns and sheared block structures (Figs 1c and 1e2 and Supplementary information 2.2 & 2.3). This observation proves that they propagate towards the nucleus interior, being part of a same network, and proves that shearing occurs inside the nucleus, down to at least several hundreds-of-meters, i.e. the maximum neck depth (Fig. 3).

In both hemispheres, the neck borders exhibit cliff faces (Supplementary Figs 7c-d, 9b) that mainly follow the 2 preferential directions of fractures (Supplementary Fig. 8b). These particular cliffs are thus the remains of fractures walls, where the opposite side has been eroded. Therefore, the nucleus material breakdown, and then erosion, in the neck (i.e. neck's trough shaping) has been, at least partially, caused by shear deformation. Indeed, mechanical breakdown may act or have acted as an amplification/facilitating process for increasing sublimation, by exposing more pristine, non-dust-covered material, more prone to sublimation and may also have allowed block removal and transport/escape.

These observations imply that finally, from the neck border to the neck centre/bottom, we therefore observe the same shear structure over hundreds-of-metres depth, at different evolution levels, driven by mechanical erosion along underlying and pre-existing fractures (Fig.3). It goes from fractured with little mechanical erosion in the neck borders (1 in Fig. 3b-c), to partially eroded in Bakhu (2 in Fig. 3b-c), and finally to highly sheared/crushed and eroded, forming flattened areas, in the neck centre (3 in Fig. 3b-c). These 3D observations necessarily imply that:

(i) the nucleus interior is structured by decametre-to-hectometre fracture networks, (ii) the nucleus material remains sufficiently brittle below the surface to allow fracturing, even at several-hundreds-of-meters depths, (iii) although the nucleus exhibits layering, it is mechanically homogenous enough for fractures to propagate freely, without being stopped or damped by mechanical boundaries, i.e. that layers do not show sharp mechanical contrasts.

Implications for the evolution of bilobate comets

With these results, we can now propose a chronology explaining the erosion and shape evolution of 67P (Fig.4).

Step 1 – Following ⁴, 67P acquired its bilobate shape roughly 4.5 Gyrs ago, in the primordial or scattered disk, with the low-velocity accretion of two cometesimals^{4,5} (Fig. 4a). Alternatively, the bilobate shape could also originate from a more recent catastrophic collision and re-accumulation event ⁶, although the probability of such an event drops to < 5% after 3.5 Gyr BP³⁶, when the Kuiper belt acquired its current object density³⁷ (Fig. 4a).

Step 2 – Then, due to torque-stress at the lobes' boundary, which originates from an initial asymmetry of the nucleus, shear deformation starts all around 67P, leading to pervasive fracturing (i.e. type 2 lineaments, Fig. 4b). This stress originates from the geometry of the nucleus, but we cannot exclude that several later close encounters with giant planets¹ provided additional tidal stresses. Continuing shear deformation, possibly over Gyr's, progressively increases the fracturing level (length, connections...), hence producing even more broken/damaged material in the neck.

Step 3 – Hundred-thousands-to-millions of years ago¹, 67P entered the giant planet region. Its temperature slowly increases and sublimation of the most volatile ices (CO, N₂ and CO₂) starts (Fig. 4c). The still-ongoing mechanical breakdown induced by shearing continues to weaken the

nucleus material, setting the conditions for differential erosion focused on the lobe boundary, increasing its depth, and forming a deep “neck” (Fig 4c).

Along with broad volatile sublimation, outbursts induced by fracturing³⁸ (or fracture reactivation), driven by sudden confinement/pressure loss, could have also contributed to ejecting and eroding the fractured loose blocks from the nucleus, enhancing the preferential neck erosion. This process is especially plausible and most efficient for smaller blocks in the crushed-material of the neck centre. This leads to increasing cliff heights surrounding the neck, therefore leads to more probability of cliff collapse³⁹ and block fragmentation, exposing ice rich materials to the surface, which amplifies even more the preferential erosion in the neck.

Step 4 – Ultimately, 67P reaches the inner solar system and its Jupiter-family comet orbit, with a perihelion distance, q , inside 5 AU. At this distance, the sublimation of water starts, leading to broad erosion by sublimation, which becomes the dominant process here (Fig. 4d). Reaching its current orbit ($q=1.2$ AU), the erosion is typically 0.4-1 m per orbit^{40,41}. This significant erosion primarily affects the most insolated areas at perihelion, i.e. the SH⁴⁰, and more precisely the lobes rather than the neck, where projected shadows limit insolation. It is responsible for the large depth difference between the SH (≈ 450 m) and NH (≈ 930 m), by flattening the SH neck’s flanks, giving 67P its current North-South asymmetric shape (Fig 4e).

The above scenario and conclusions on the internal structure are not restricted to 67P and can apply to other bilobate comets, which is likely a common shape among cometary nuclei, and could explain previous (even non-directly observed) nucleus splitting⁴². As shown by the recent New Horizon mission, active geological processes exist in the Kuiper belt, on long time scale, and comets are no exception. Finally, this work also brings new perspectives on the comet activity phenomenon, where deep propagating fracture and fault growth could trigger outbursts³⁸, even at large (>5 a.u.) heliocentric distances⁴³.

References:

- 1 Duncan, M., Levison, H. & Dones, L. Dynamical evolution of ecliptic comets. *Comets II*, 193-204 (2004).
- 2 Sunshine, J. M., Thomas, N., El-Maarry, M. R. & Farnham, T. L. Evidence for geologic processes on comets. *Journal of Geophysical Research-Planets* 121, 2194-2210, doi:10.1002/2016je005119 (2016).
- 3 Massironi, M. et al. Two independent and primitive envelopes of the bilobate nucleus of comet 67P. *Nature* 526, 402-+, doi:10.1038/nature15511 (2015).
- 4 Davidsson, B. J. R. et al. The primordial nucleus of comet 67P/Churyumov-Gerasimenko. *Astronomy & Astrophysics* 592, doi:10.1051/0004-6361/201526968 (2016).
- 5 Hirabayashi, M. et al. Fission and reconfiguration of bilobate comets as revealed by 67P/Churyumov-Gerasimenko. *Nature* 534, 352-+, doi:10.1038/nature17670 (2016).
- 6 Schwartz, S. R. *et al.* Catastrophic disruptions as the origin of bilobate comets. *Nature Astronomy* 2, 379-382, doi:10.1038/s41550-018-0395-2 (2018).
- 7 Jutzi, M. & Benz, W. Formation of bi-lobed shapes by sub-catastrophic collisions A late origin of comet 67P's structure. *Astronomy & Astrophysics* 597, doi:10.1051/0004-6361/201628964 (2017).
- 8 Keller, H. U. et al. OSIRIS – The Scientific Camera System Onboard Rosetta. *Space Science Reviews* 128, 433-506, doi:10.1007/s11214-006-9128-4 (2007).

252 9 El-Maarry, M. R. et al. Fractures on comet 67P/Churyumov-Gerasimenko observed by
253 Rosetta/OSIRIS. *Geophysical Research Letters* 42, 5170-5178, doi:10.1002/2015gl064500
254 (2015).

255 10 Thomas, N. et al. The morphological diversity of comet 67P/Churyumov-Gerasimenko.
256 *Science* 347, doi:10.1126/science.aaa0440 (2015).

257 11 Auger, A. T. et al. Meter-scale thermal contraction crack polygons on the nucleus of
258 comet 67P/Churyumov-Gerasimenko. *Icarus*, doi:https://doi.org/10.1016/j.icarus.2017.09.037
259 (2017).

260 12 Attree, N. *et al.* Thermal fracturing on comets. *A&A* **610** (2018).
261

262 13 Lee, J. C. et al. Geomorphological mapping of comet 67P/Churyumov-Gerasimenko's
263 Southern hemisphere. *Monthly Notices of the Royal Astronomical Society* 462, S573-S592,
264 doi:10.1093/mnras/stx450 (2016).

265 14 Penasa, L. a. M. M. a. N. G. a. S. E. a. F. S. a. P. M. a. L. A. a. P. F. a. S. F. a. A three
266 dimensional modelling of the layered structure of comet 67P/Churyumov-Gerasimenko. *Monthly*
267 *Notices of the Royal Astronomical Society*, stx2899, doi:10.1093/mnras/stx2899 (2017).

268 15 Lyell, C. & Deshayes, G. P. *Principles of Geology: Being an Attempt to Explain the*
269 *Former Changes of the Earth's Surface, by Reference to Causes Now in Operation.* (J. Murray,
270 1830).

271 16 Steno, N. *De Solido Intra Solidum Naturaliter Contento.*, Vol. 78 (1669).

272 17 Twiss, R. J. & Moores, E. M. *Structural geology.* (Macmillan, 1992).

273 18 Rao, G. et al. Co-seismic Riedel shear structures produced by the 2010 M-w 6.9 Yushu
274 earthquake, central Tibetan Plateau, China. *Tectonophysics* 507, 86-94,
275 doi:10.1016/j.tecto.2011.05.011 (2011).

276 19 Matonti, C., Lamarche, J., Guglielmi, Y. & Marié, L. Structural and petrophysical
277 characterization of mixed conduit/seal fault zones in carbonates: Example from the Castellás fault
278 (SE France). *Journal of Structural Geology* 39, 103-121, doi:10.1016/j.jsg.2012.03.003 (2012).

279 20 Peacock, D. C. P., Nixon, C. W., Rotevatn, A., Sanderson, D. J. & Zuluaga, L. F.
280 Glossary of fault and other fracture networks. *Journal of Structural Geology* 92, 12-29,
281 doi:10.1016/j.jsg.2016.09.008 (2016).

282 21 Mukherjee, S. *Atlas of Structural Geology*. (Elsevier Science, 2015).

283 22 Mitchell, T. M. & Faulkner, D. R. The nature and origin of off-fault damage surrounding
284 strike-slip fault zones with a wide range of displacements: A field study from the Atacama fault
285 system, northern Chile. *Journal of Structural Geology* 31, 802-816, doi:10.1016/j.jsg.2009.05.002
286 (2009).

287 23 Soliva, R. and Schultz, R. A. Distributed and localized faulting in extensional settings:
288 Insight from the North Ethiopian Rift–Afar transition area. *Tectonics* 27,
289 doi:10.1029/2007TC002148.

290 24 Cladouhos, T. T. & Marrett, R. Are fault growth and linkage models consistent with
291 power-law distributions of fault lengths? *Journal of Structural Geology* 18, 281-293,
292 doi:10.1016/s0191-8141(96)80050-2 (1996).

293 25 Preusker, F. et al. The global meter-level shape model of comet 67P/Churyumov-
294 Gerasimenko. *Astronomy & Astrophysics*, 607, L1, doi:10.1051/0004-6361/201731798 (2017)

295 26 Riedel, W. *Zur Mechanik Geologischer Brucherscheinungen* Central bl. F. Min. Geol.
296 Und Pal 8, 354-368 (1929).

297 27 Bartlett, W. L., Friedman, M. & Logan, J. M. Experimental folding and faulting of rocks
298 under confining pressure .9. wrench faults in limestone layers. *Tectonophysics* 79, 255-277,
299 doi:10.1016/0040-1951(81)90116-5 (1981).

300 28 Ahlgren, S. G. The nucleation and evolution of Riedel shear zones as deformation bands
301 in porous sandstone. *Journal of Structural Geology* 23, 1203-1214, doi:10.1016/s0191-
302 8141(00)00183-8 (2001).

303 29 Groussin, O. et al. Gravitational slopes, geomorphology, and material strengths of the
304 nucleus of comet 67P/Churyumov-Gerasimenko from OSIRIS observations. *Astronomy &*
305 *Astrophysics* 583, doi:10.1051/0004-6361/201526379 (2015).

306 30 Vincent, J. B. et al. Constraints on cometary surface evolution derived from a statistical
307 analysis of 67P's topography. *Monthly Notices of the Royal Astronomical Society* 469, S329-
308 S338, doi:10.1093/mnras/stx1691 (2017).

309 31 Hatton, C. G., Main, I. G. & Meredith, P. G. Non-universal scaling of fracture length and
310 opening displacement. *Nature* 367, 160-162 (1994).

311 32 Hviid, S., Hüttig, C., Groussin, O., Mottola, S., Keller, H. U., et al. A Creaking and
312 Cracking Comet. *AAS/Division for Planetary Sciences Meeting Abstracts*, Vol. 48,
313 *AAS/Division for Planetary Sciences Meeting Abstracts*, 211.05 (2016).

314 33 Attree, N. *et al.* Tensile strength of 67P/Churyumov–Gerasimenko nucleus material from
315 overhangs. *A&A* **611** (2018).

316 34 Basilevsky, A. T. et al. Estimating the strength of the nucleus material of comet 67P
317 Churyumov–Gerasimenko. *Solar System Research* 50, 225-234,
318 doi:10.1134/s0038094616040018 (2016).

319 35 Hooker, J. N., Laubach, S. E. & Marrett, R. Fracture-aperture size—frequency, spatial
320 distribution, and growth processes in strata-bounded and non-strata-bounded fractures, Cambrian
321 Mesón Group, NW Argentina. *Journal of Structural Geology* 54, 54-71,
322 doi:https://doi.org/10.1016/j.jsg.2013.06.011 (2013).

323 36 Durda, D. D. & Stern, S. A. Collision Rates in the Present-Day Kuiper Belt and Centaur
324 Regions: Applications to Surface Activation and Modification on Comets, Kuiper Belt Objects,

Centaurs, and Pluto–Charon. *Icarus* 145, 220-229, doi:<https://doi.org/10.1006/icar.1999.6333>
(2000).³⁷ Weissman, P. R. & Levison, H. F. in *Pluto and Charon* 559 (1997).³⁸ Skorov,
Y. V., Rezac, L., Hartogh, P., Bazilevsky, A. T. & Keller, H. U. A model of short-lived outbursts
on the 67P from fractured terrains. *A&A* 593, A76 (2016).
³⁹ Pajola, M. et al. The pristine interior of comet 67P revealed by the combined Aswan
outburst and cliff collapse. *Nature Astronomy* 1, doi:[10.1038/s41550-017-0092](https://doi.org/10.1038/s41550-017-0092) (2017).
⁴⁰ Lai, I. L. et al. Gas outflow and dust transport of comet 67P/Churyumov-Gerasimenko.
Monthly Notices of the Royal Astronomical Society 462, S533-S546, doi:[10.1093/mnras/stx332](https://doi.org/10.1093/mnras/stx332)
(2016).
⁴¹ Keller, H. U. et al. Insolation, erosion, and morphology of comet 67P/Churyumov-
Gerasimenko. *A&A* 583, A34 (2015).
⁴² Boehnhardt, H. in *Comets II* (ed M.C. and Keller Festou, H.U. and Weaver, H.A.) 301-
316 (2004).
⁴³ Sekanina, Z., Larson, S. M., Hainaut, O., Smette, A. & West, R. M. Major outburst of
periodic Comet Halley at a heliocentric distance of 14 AU. *Astronomy and Astrophysics* 263,
367-386 (1992).

Acknowledgments

OSIRIS was built by a consortium of the Max-Planck-Institut für Sonnensystemforschung, Göttingen, Germany; the CISAS University of Padova, Italy; the Laboratoire d'Astrophysique de Marseille, France; the Instituto de Astrofísica de Andalucía, CSIC, Granada, Spain; the Research and Scientific Support Department of the ESA, Noordwijk, Netherlands; the Instituto Nacional de Técnica Aeroespacial, Madrid, Spain; the Universidad Politécnica de Madrid, Spain; the Department of Physics and Astronomy of Uppsala University, Sweden; and the Institut für Datentechnik und Kommunikationsnetze der Technischen Universität Braunschweig, Germany. The support of the national funding agencies of Germany (DLR), France (CNES), Italy (ASI), Spain (MEC), Sweden (SNSB), and the ESA Technical Directorate is gratefully acknowledged. We thank the Rosetta Science Operations Centre and the Rosetta Mission Operations Centre for the successful rendezvous with comet 67P/Churyumov–Gerasimenko. The authors would also like to thank the ParadigmGeo company for their support in providing the gOcad software, V. A. La Bruna for the interesting Structural Geology discussions related to this study, and Y. Guglielmi for his advices on the submission.

Data Availability

All the images analysed during the current study are available in the ESA-PSA repository (<https://archives.esac.esa.int/psa>). The data that support the findings of this study are in the supplementary information section and available from the corresponding author upon reasonable request (C.Matonti; matonti@cerege.fr).

Author contributions

C.M led this study, mapped the lineaments, performed geological interpretation and wrote most of the manuscript. N.A performed the 3D projection of the lineaments as well as the statistical calculations and interpretations, and participated to the manuscript writing. O.G contributed significantly to the interpretations and to the manuscript writing. L.J provided local and global 3D models and developed tool for images selection and data projection. S.V contributed to the 3D statistical analysis and data importing to the Gocad software. S.H provided the 3D stress model for 67P. S.B contributed to improved design of the study, interpretations and manuscript. D.N contributed to the local and global 3D shape model creation. A-T.A contributed to the image selection and geological interpretation. P.L provided Stereo anaglyph images used for interpretation.

H.S., C.B., P.L., R.R., D.K. and H.R. are the lead scientists of the OSIRIS project. The other authors are all co-investigators who built and ran this instrument and made the observations possible, and associates and assistants who participated in the study.

Figures Captions:

Figure 1: Fracture pattern on 67P's SH showing fracture interpretations and comparison with typical Earth analogues/equivalents. a. NAC_2016-01-28T05.33.00.986Z_ID30_1397549000_F22 image, showing neck borders and centre regions. b. NAC_2016-01-30T08.28.39.721Z_ID30_1397549200_F22, Wosret neck border (b1) with interpreted layers (green) and digitalized fracture lineaments (red), showing anastomosing and highly interconnected pattern (b2). Earth example of a fault-zone showing similar anastomosing pattern and following typical Riedel-shear structure (with R&P planes)¹⁸ (b3). c. NAC_2016-01-

27T18.20.08.974Z_ID30_1397549000_F22 cropped image, showing close-up of the neck centre exhibiting ridges and chaotic zones. d. Zoom on the neck border (d1) with fractures (red) crosscutting possible layers (green), highlighting the occurrence of a dense, oblique fracture set located in-between longer fractures (d2). Example of anastomosing shear fault-zone with sinistral-slip motion, including oblique shear-fractures between minor fault and sheared block¹⁹ (d3). e. Close-up on brittle material ridges in the neck bottom (e1), affected by oblique fractures (in red) and chaotic/unstructured crushed zones (in grey) (e2). Image of a sheared rock-block, pinched between two minor faults, exhibiting oblique Riedel-shear fractures (e3, from²¹).

Figure 2: Fracture length distribution and directions statistics. a. Cumulative length distribution plot of all the digitalized fracture. The distribution follows a power law between 30-40 and 250 m (see methods). b Cumulative length distribution of meter scale polygonal fractures (data from¹¹) showing no evidence of a power law distribution, but exponential distribution, contrarily to tectonic shear (linked or reactivated) fractures and faults which classically exhibit power law distribution. c. Polar plot of the longest fractures ($L > 100$ m) average directions compared to the neck middle plane (θ angle = 0° means parallel to the neck). It shows scattering mainly in a 35° range. d. Polar plot of the shorter fracture ($L < 100$ m) directions compared to the neck middle plane. It shows large scattering over a $> 100^\circ$ range.

Figure 3: Block diagram revealing 67P's fractured internal structure and its evolution through increasing mechanical erosion. a. Location of the 3 views on 67P's nucleus. b. NAC images illustrating increasing erosion level along a unique fractured structure. c. Block diagrams. 1: initial, non (mechanically) eroded, topographic surface, as observed in Wosret. 2: partially

eroded topographic surface, cut along the pre-existing fracture directions and dip angles, as observed in Hapi equatorial area (Bakhu). 3. Highly flattened surface topography, eroded along the same fracture network with increased deformation in the Neck's centre, forming lenticular shaped ridge and crushed chaotic zones, as observed in Anhur/Sobek regions.

Figure 4: Chronology of the evolution of the shape of 67P (from primordial or collisional later event), showing the effects of the two complementary erosion processes (mechanical erosion and sublimation erosion). It highlights the contrast between the shear deformation, acting in the neck over long time scales (Gy's), and the sublimation erosion, acting on the broad nucleus over shorter time scales (My's). Double red-arrows are the symbol for shear deformation, illustrating torque at the neck, and do not imply a sense of rotation.

Methods

10 OSIRIS-NAC images, acquired between 8.3 and 70 km from the nucleus centre of mass, were used for this work in order to digitalise 2879 lineaments. Digitalisation was performed using the vector-based Adobe illustrator drawing software. Image resolution and size at the nucleus surface range respectively from 0.33 -1.23 m/px and 0.69 - 2.79 km. Digitalised lineaments are polyline objects made only of straight line combinations (Supplementary Fig. 2a). Lineaments were exported in .svg format and projected onto the SPG-SHAP7²⁵ nucleus model, using the known geometry of OSIRIS images⁴⁴ (Supplementary Fig. 2b). A neck axis plane was defined, using the midplane of the neck border coordinates from²⁵, and the average distance and direction (weighted by segment lengths) of each lineament were computed relative to this.

The fracture cumulative length distribution fit was performed following classic recommendations from⁴⁵. Our data set is composed of more than 200 measurements and ranges over 2 orders of magnitude. Nevertheless, for power law exponent determination, we only sampled fractures inside 0.5 to 25% of the image actual size, in order to avoid typical issues such as: (i) truncation effect, due to image resolution limits; (ii) length bias or censoring effect, due to the size of images/sampling area compared to the size of longest fractures; and (iii) statistical effect due to undersampling of the largest objects.

Cliff directions have been computed using the Gocad software (Paradigmgeo), by drawing lines parallel to the cliffs directly onto the shape model mesh triangles. Parallel-view/orthographic view was used in order to avoid perspective/parallax effect bias. Anaglyph 3D view mode has been used to better estimate depth, in order to accurately draw the line on the cliffs, minimizing error in cliffs directions.

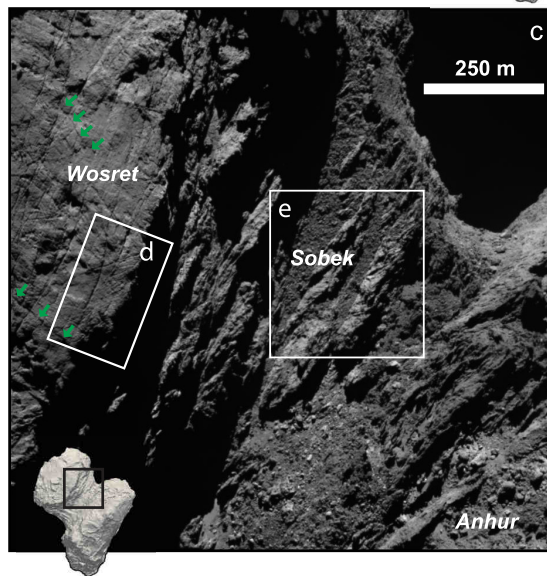
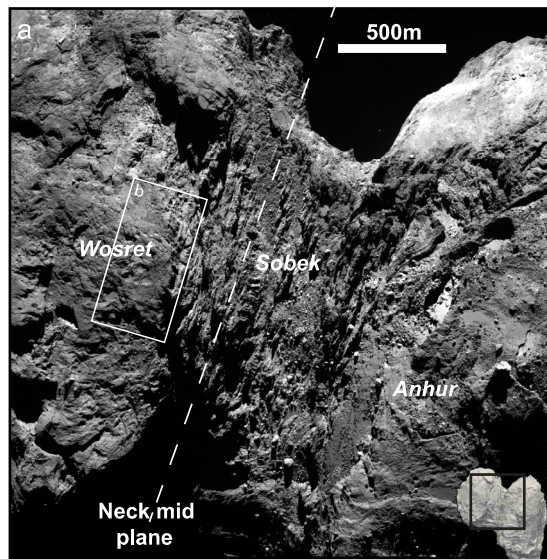
The full stress tensor for 67P was computed taking into account gravity and rotational forces, considering a Young's modulus value of 50 MPa and a Poisson ratio of 0.32³². The stress model was computed using a finite element mesh composed of 2 million cells, and principal stress values and directions were mapped onto the cg-dlr_spg-shap7-v1.0 model²⁵.

References only in Methods:

44 Gaskell, R. W. a. B.-J. H. A. O. S. a. S. D. J. a. K. A. S. a. M. T. a. A. B. Characterizing and navigating small bodies with imaging data. *Meteoritics & Planetary Science* 43, 1049--1061, doi:10.1111/j.1945-5100.2008.tb00692.x (2008).

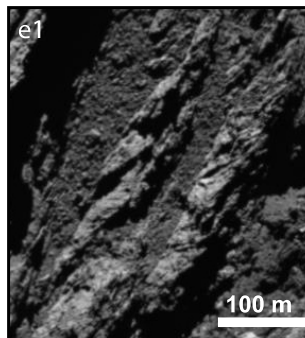
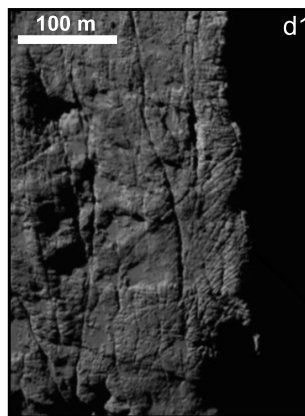
45 Bonnet, E. a. B. O. a. O. N. E. a. D. P. a. M. I. a. C. P. a. B. B. Scaling of fracture systems in geological media. *Reviews of Geophysics* 39, 347--383, doi:10.1029/1999RG000074 (2001).

Full images

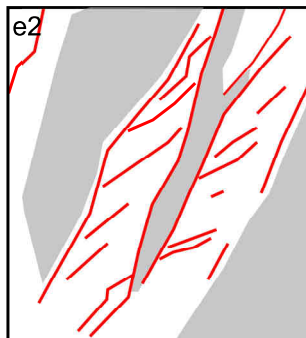
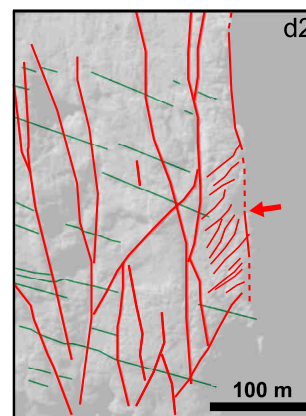
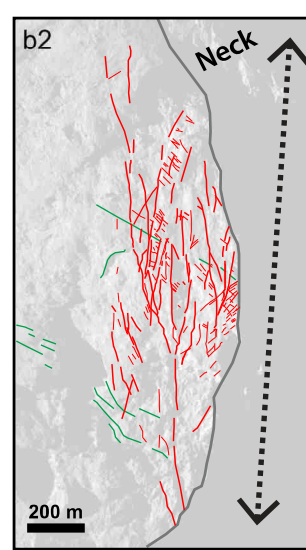


- Possible Layers
- Fractures
- ↔ Interpreted Layers lineament location
- Chaotic zones
- Nucleus topography
- ↔ Shear motion direction

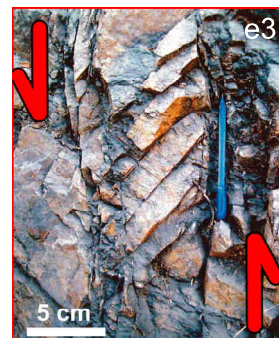
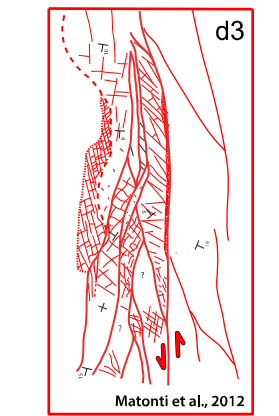
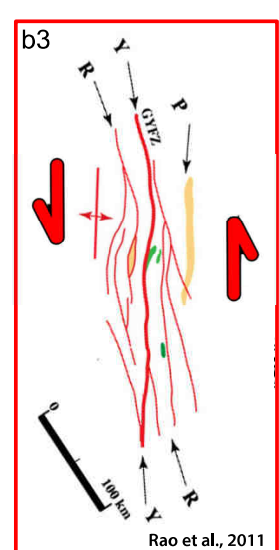
Inset images



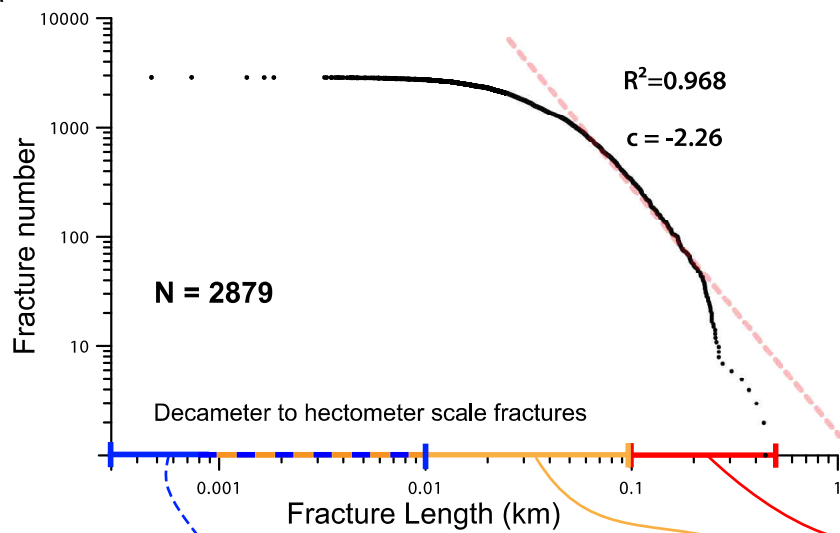
Pattern



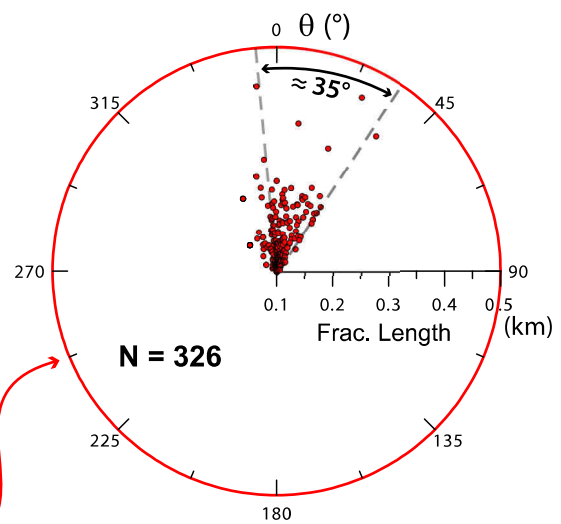
Earth analogues



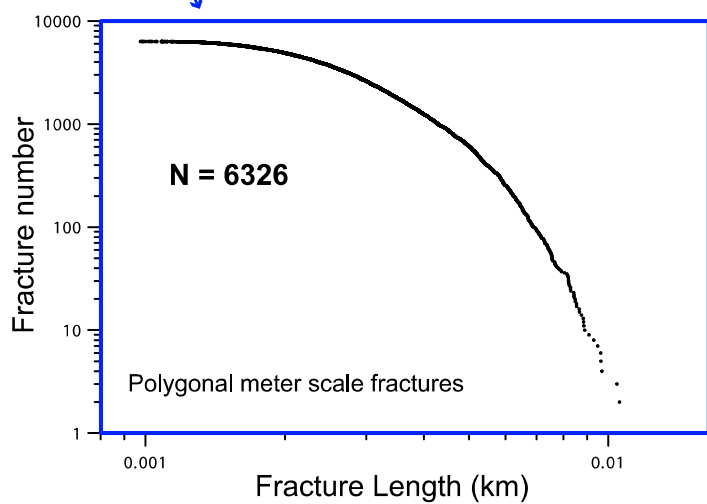
a



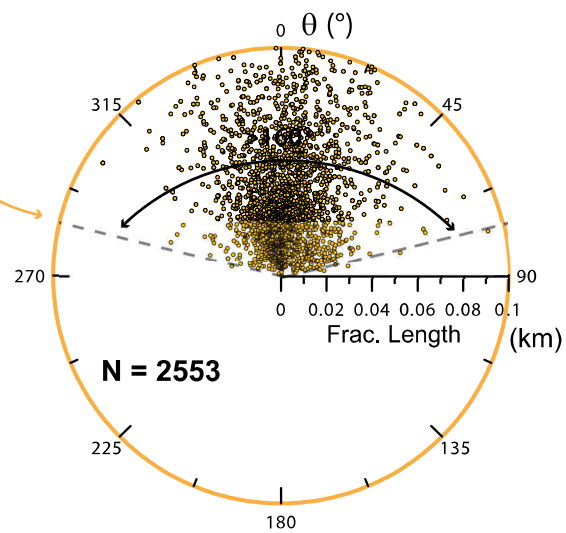
c



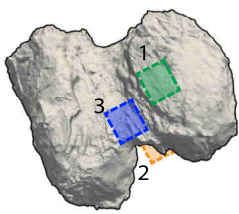
b



d

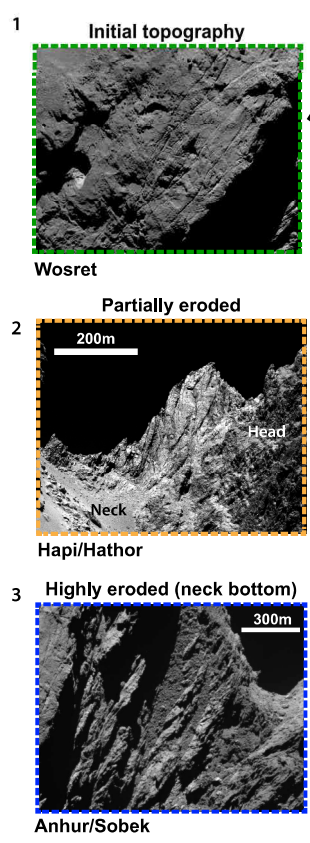


a

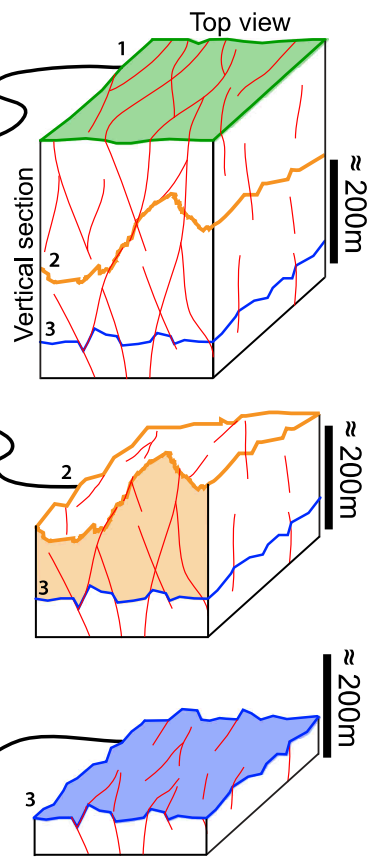


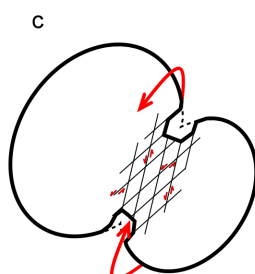
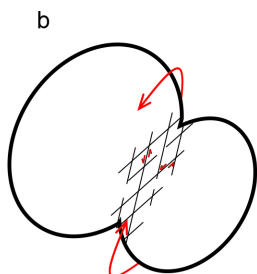
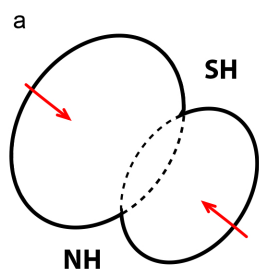
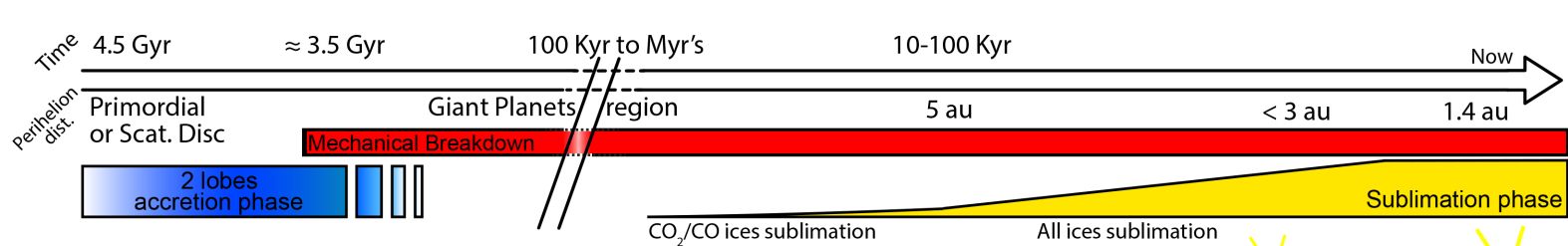
- View locations on the nucleus
- Fractures Lineaments
- Nucleus current topography surfaces

b

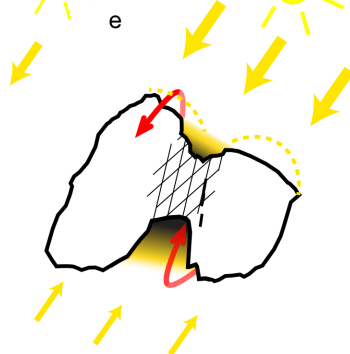
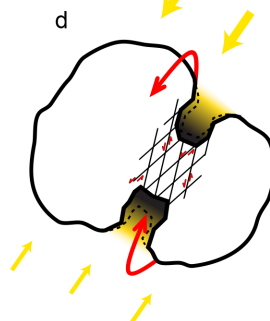


c





Mechanical erosion >> Sublimation erosion



Sublimation erosion >> Mechanical erosion